Modeling Bulbar-onset ALS using iPSC-derived Motor Neurons

Lauren Stoller

Nicole Teaney, Dr. Nisha Iyer

Laidlaw Undergraduate Research and Leadership Program

Iyer Lab, Department of Biomedical Engineering, Tufts University

Abstract

Amyotrophic Lateral Sclerosis (ALS) is a devastating neurodegenerative disease with no cure or universal effective treatment, complicated by multiple axes of heterogeneity, including onset location and genetic background; there are over 40 known gene mutations associated with ALS. Bulbar-onset disease, associated with initial degeneration of motor neurons in the hindbrain, is significantly more aggressive than other subtypes, and whether this reflects an intrinsic, cellular-level vulnerability in hindbrain cells compared to spinal ones remains unknown. Resolving this question with *in-vitro* disease modeling is crucial for developing effective therapeutics, particularly as recent precision medicine successes, e.g., tofersen, demonstrate the promise of subtype-specific treatment. However, most existing induced pluripotent stem cell (iPSC)-derived motor neuron models are generically spinal rather than region-specific, rendering them unable to test whether regional identity affects disease presentation. While iPSC-derived models have advanced our understanding of individual ALS-associated mutations, these approaches have not yet incorporated a hindbrain-specific regional identity to directly model bulbar-onset disease. This project aims to address that gap by generating hindbrain-patterned motor neurons from a healthy control (Kolf2.1J) line and two relevant mutant lines (FUS and SOD1), then examining cellular electrophysiological phenotypes with multielectrode array (MEA) analysis. Efficient differentiation of a pure motor neuron model was validated through immunocytochemistry (ICC) staining and quantification at both the ventral progenitor and mature motor neuron stages. MEA analysis did not reveal significant differences between ALS genotypes, however early hyperactive phenotypes and differences in neuronal maturation trajectories as seen through network synchrony were observed in both ALS models relative to the healthy control. Though more work is needed to uncover more disease-relevant phenotypes (e.g., metabolism differences) and distinctions between genotypes, this work constitutes a region-specific iPSC-derived motor neuron platform for exploring genotype-region interactions in ALS, providing a foundation for future studies examining bulbar disease characterization and drug screenings targeted for bulbar-onset disease.

Introduction

Amyotrophic Lateral Sclerosis (ALS) is a fatal neurodegenerative disease involving progressive degradation and death of both upper and lower motor neurons in the brain, brainstem, and spinal cord[1]. Symptoms include gradual loss of motor function corresponding with disease stage, beginning with weakness, cramping, and spasticity, or abnormal muscle stiffness and contraction[2]. Muscles atrophy over time, leading to difficulty with tasks ranging from precise skills to routine daily activities including walking, speech, swallowing, and breathing. Cognitive and emotional changes have also been noted in some cases. Though time between symptom onset and death varies widely across patient populations and disease subtypes, median survival rests around 30 months post-symptom onset, with patients most often experiencing fatal respiratory failure following death of neurons controlling breathing pathways[3,4]. ALS is a relatively rare disease with a global prevalence of approximately 5-8 per

100,000 people, though this figure varies widely between countries[5]. Despite its rarity, ALS shares similar pathological signatures with other neurodegenerative diseases such as Alzheimer's and Parkinson's diseases, as well as frontotemporal dementia, making this disease a valuable target for research efforts, as findings may be applicable across many neurological deficits[6]. Additionally, the fast disease progression and absence of effective cure, treatment, or even a unified mechanistic explanation of disease pathology associated with ALS make it a pressing target for research.

ALS is typically categorized into two distinct clinical presentations depending on its location of onset. Spinal-onset ALS represents most cases, with neuron deterioration beginning in the spinal cord and resulting in limb weakness and loss of fine motor skills as early observable symptoms[7]. Conversely, bulbar-onset ALS represents only 25-30% of all cases, first affecting neurons of the cranial motor nuclei and corticobulbar pathways, two brainstem pathways enervating muscles of the face, neck, and head, controlling both voluntary and involuntary movements in these areas. This disease subtype causes early symptoms such as dysarthria or dysphagia, or impairments of speech and swallowing, respectively. Bulbar-onset ALS is known to have a significantly more aggressive symptom onset and worse prognosis compared to limb-onset, though the reason behind this disparity is unknown[5,8,9]. The difference could be purely tied to the fact that many critical muscles are enervated by bulbar motor neurons, and the consequences of losing function here are more detrimental to quality of life compared to limb-onset disease. However, the possibility of an intrinsic, cellular-level difference between spinal and brainstem motor neurons causing the bulbar region to be more vulnerable to disease-related degeneration cannot be ruled out.

Another factor complicating endeavors to learn more about ALS mechanisms is its genetic heterogeneity, a hallmark of the disease. A vast majority, approximately 90% of all cases, are sporadic, with disease likely resulting from an interplay of genetic risk and environmental factors rather than family history[10,11]. The remaining 10% of cases are familial and related to inherited pathogenic mutations in one or more of over 40 identified genes. Of these mutations, a few common and well-known ones include SOD1, a gene encoding cytoplasmic antioxidant enzyme superoxide dismutase 1; TARDBP, encoding the DNA-binding protein TDP-43 (TAR DNA-binding protein 43); FUS, encoding the RNA-binding protein fused in sarcoma; and C9orf72, encoding the C9orf72 protein involved with autophagy, or cellular waste recycling, and membrane trafficking[11]. Each of these mutations, and combinations thereof, are thought to cause ALS pathology through distinct cellular-level mechanisms. Understanding these mechanisms through *in-vitro* disease modeling and thorough characterization of disease-relevant phenotypes is crucial for developing therapeutic interventions targeting ALS.

This extreme heterogeneity, along with biological differences between *in-vitro* models, animal models and human disease, have resulted in very poor translation of research findings from preclinical models to clinical trial. Human iPSC-derived models offer a complementary approach to animal models by enabling the study of disease-associated mutations in a human context while also being able to model specific neuronal populations implicated in disease. A

therapeutic candidate targeting one mutation's pathogenic mechanism is unlikely to be effective for patients whose disease arises from a distinct mutation and thus different disease pathway. In mixed-genotype clinical trials, this creates the illusion that the candidate being tested is far less effective. The solution to this failure in translation may be genotype- and mechanism-specific medications. To provide an example, the antisense oligonucleotide tofersen, a medication targeting SOD1 mRNA, missed its primary efficacy endpoint in the Phase III VALOR trial, failing to significantly improve clinical outcomes relative to placebo after 26 weeks[12]. However, on the cellular level, tofersen did cause significant reductions in SOD1 protein and neurofilament light chain, two biomarkers of disease progression. Despite its clinical trial failure, the biomarker success granted tofersen FDA accelerated approval in 2023 for patients with SOD1-ALS[13]. This demonstrates both the importance of considering genotype in treatment design, as well as the ongoing challenge of demonstrating clinical efficiency in ALS trials. This reinforces a need for robust, genotype-specific *in-vitro* motor neuron systems to identify and validate new therapeutics before going to clinical trial.

Though much work has been done to create these *in-vitro* systems for studying ALS genotype effects on motor neuron dysfunction, this alone cannot resolve the first source of heterogeneity discussed above: whether bulbar motor neurons carry an intrinsic vulnerability to degeneration. Most stem cell-derived motor neuron models do not carry a regional identity and are generically spinal by nature, thus making them incapable of answering that question, in spite of evidence suggesting motor neurons from different regions are biologically distinct[14–16]. Addressing both the clinical onset and genetic axes of ALS heterogeneity therefore requires model systems specific to both genotype and regional identity. This project aims to fill this largely unexplored gap by developing and validating an induced pluripotent stem cell (iPSC)-derived motor neuron model specific to the hindbrain in order to observe ALS cellular-level phenotypes in a model replicating bulbar-onset disease. Though recent studies have investigated contributions of cell types other than motor neurons, such as microglia and oligodendrocytes, to ALS, this project focuses solely on motor neuron phenotypes[17,18]. To return to the genotype question, out of all ALS-associated mutations, two have been chosen for this project: SOD1 and FUS. SOD1 was the first ALS-associated mutation to be identified and is the most thoroughly characterized in literature[19]. SOD1 mutations are also highly correlated with aggressive, spinal-onset disease. In contrast, FUS is a comparatively rare ALS mutation with a strong correlation with aggressive, bulbar-onset disease[20]. Additionally, both mutations investigated in this project are heterozygous, an important distinction as the majority of aggressive familial ALS cases involve heterozygous mutations[19,20]. Pairing these two mutations with region-specific motor neurons leads to our hypothesis: combining bulbar-region motor neurons with a bulbar-associated mutation may result in more severe disease phenotypes compared to the mismatched situation of bulbar-region motor neurons with a spinal-associated mutation.

In order to test this hypothesis, three lines of iPSCs, a healthy parent line, Kolf2.1J, and two gene-edited lines with heterozygous FUS and SOD1 mutations, are differentiated into motor neurons by a classical developmental biology protocol (*Fig. 1A*). Cells from all three lines were

first converted to neuromesodermal progenitors (NMPs). At this stage of differentiation, the regional identity these progenitors ultimately adopt is controlled by Wnt signaling, a molecular pathway influencing rostral-caudal patterning in a dose-dependent manner[21,22]. Brief or weak Wnt signaling leads to more rostral (towards the head) identities, while long or strong Wnt signaling leads to more caudal (towards the tail) identities. To give rise to hindbrain-region, or bulbar motor neurons, iPSCs are treated with a relatively brief, 72-hour dose of Wnt-activating compounds to achieve NMPs on the very rostral end of the spectrum. From there, NMPs were treated with small-molecule morphogens imitating embryonic development to become spinal progenitors, followed by ventral progenitors, as the ventral domain gives rise to motor neurons as opposed to other subtypes, e.g., sensory or interneurons[23]. Treatment with a different set of supplements, including DAPT, a compound inhibiting Notch signaling to trigger neuronal identity, was then used to shift ventral progenitors towards a neuronal fate, first inducing motor neuron identity, then finally producing mature motor neurons[24].

This project particularly concerns the final steps in motor neuron production, from ventral progenitors through motor neuron induction and maturation. At the ventral progenitor stage, differentiation efficiency was assessed through ICC staining for and quantification of transcription factors Olig2 and NKX6.1, canonical ventral progenitor markers preceding motor neuron specification[25]. At the mature motor neuron stage, identity was further validated by staining for markers ISL1, ChAT, TUJ1, and HB9, all either neuronal or motor-neuron-specific indicators[26]. Neurons were also stained for Chx10, a marker of excitatory interneurons, to assess culture purity, as we aim to obtain a pure motor neuron culture with no supporting cells[27]. Establishing robust biomarker imaging and quantification pipelines is necessary in order to attribute any downstream disease-relevant phenotype observations to genotype or regional identity, as opposed to differences in differentiation efficiency. Following neuronal induction, immature motor neurons were plated onto multi-electrode arrays (MEA), a specialized cell culture and functional assay platform used for longitudinal, non-invasive recording of network-level electrophysiological activity over the course of neuronal maturation. Unlike other electrophysiological assays such as single-cell patch clamp, MEA tracks activity across entire groups of neurons over days to weeks, enabling high-level pattern identification over the course of maturation and across genotypes[28]. MEA recordings may capture spontaneous activity, including key metrics such as mean firing rate, network burst frequency, an inter-burst-interval variability, as well as network response to electrical evocation, in which neurons are given an external input and strength and synchrony of network response is measured. Together, these metrics provide a wealth of information on neuronal network health, synchrony, and activity level, which may reveal disease-relevant phenotypes not otherwise observable, such as cytotoxic hyperactivity, implicated in many ALS genotypes.

Overall, developing a model for bulbar-onset ALS using region-specific hindbrain motor neurons derived from gene-edited iPSCs, validating model efficiency using ICC staining and quantification, and evaluating early disease-relevant phenotypes via MEA electrophysiology recording constitute the aims of this project.

Materials & Methods

*Refer to *Table 1* for full reagent names, concentrations, and reference numbers.

Motor neuron differentiation from Kolf2.1J ventral progenitors

Twelve-well plates were coated with Matrigel diluted in DMEM/F-12 and incubated at 37ºC for at least 3 h before use. Banked ventral progenitors derived from Kolf2.1J parental iPSCs and gene-edited FUS and SOD1 mutant iPSCs lines were seeded at 960,000 cells/well in neural induction medium consisting of Essential 6 supplemented with 1 µg/mL laminin, 10 ng/mL BDNF, 10 ng/mL GDNF, 10 ng/mL NT3, 2% B-27, and 10 µM DAPT. CEPT cocktail (50 nM Chroman 1, 5 µM Emricasan, 1:1,000 polyamine supplement, and 0.7 µM trans-ISRIB) was included during initial plating and the first media change only. Half-media changes were performed every other day for 7 days using CEPT-free neural induction medium after the initial treatment. To reduce non-neuronal cell populations, 10 µM AraC was added on days 2 and 4.

On day 5 of neural induction, fresh MEA plates were coated with 0.1 mg/mL Poly-D-Lysine (PDL) dissolved in sterile water. These were incubated overnight at room temperature in the biosafety cabinet without UV. The next day, on day 6 of neural induction, PDL coating was aspirated and washed three times with sterile water, then dried completely. Plates were coated again with 5 µg/mL laminin and incubated overnight at 37ºC.

On day 7 of neural induction, induced motor neurons were dissociated from culture plates and re-plated on MEA plates to commence maturation and data collection. Dissociation reagent was prepared by reconstituting 1000 units of DNase I and 100 units of papain in 6 mL of DMEM. Induction media was aspirated from culture plates. Dissociation reagent was added to wells and incubated for 5-10 minutes until cell detachment in a sheet was noticeable with the naked eye. The reaction was quenched with 10% fetal bovine serum. Neurons were pelleted via 3-minute centrifuge at 300xg. Cells were re-suspended via mechanical trituration with homemade neuron maturation media. This media consisted of Neurobasal Plus base media supplemented with 1% N2, 2% B-27 plus, 1 µM cAMP, 10 ng/mL GDNF, 10 ng/mL BDNF, 10 ng/mL NT3, 1x Glutamax, 1 µM laminin, and CEPT cocktail. Cell count was performed. Cells were plated at the very center of the coated MEA plates, on top of electrodes, at a 100,000 cell/well density. Plates were incubated for one hour before slowly adding 500 µL maturation medium in all wells. Cells were incubated overnight. The next day, day 1 of maturation, an additional 500 µL maturation medium was added to all wells. Beginning day 3 of maturation, every other day half-media changes were performed using neuron maturation media without CEPT.

Immunocytochemistry (ICC) staining and fluorescence imaging

Ventral progenitor staining and imaging:

Cells were fixed with paraformaldehyde for 10 min at room temperature, washed three times with phosphate-buffered saline (PBS), and blocked for 1 h at room temperature in blocking buffer containing PBS, normal donkey serum, and Triton X-100. Cells were then incubated overnight at 4ºC with rabbit anti-OLIG2 (1:200) and goat anti-NKX6.1 (1:500) primary antibodies diluted in blocking buffer.

Following three PBS washes, cells were incubated with species-appropriate Alexa Fluor-conjugated secondary antibodies Alexa Fluor donkey anti-rabbit 555 and Alexa Fluor donkey anti-goat 647 (1:500) for 1 h at room temperature protected from light. Secondary-only controls were processed in parallel without primary antibodies. Cells were counterstained with DAPI (1:2,000) for 5 min at room temperature, washed twice with PBS, and imaged at 10× magnification using a Molecular Devices ImageXpress high-content imaging system.

Images were post-processed in ImageJ and analyzed using CellProfiler to quantify OLIG2- and NKX6.1-positive cells relative to total DAPI-positive nuclei. The 99th percentile of fluorescence intensity from secondary-only controls was used to establish the threshold for true-positive staining. Data were plotted in R.

Neuron staining and imaging:

Cells were fixed with paraformaldehyde for 10 min at room temperature, washed three times with PBS, and blocked for 1 h at room temperature in blocking buffer containing PBS, normal donkey serum, and Triton X-100. Cells were incubated overnight at 4ºC with rabbit anti-ChAT (1:100), goat anti-ISL1 (1:500), chicken anti-TUJ1 (1:500), and either mouse anti-HB9 (1:50) or mouse anti-CHX10 (1:100) primary antibodies diluted in blocking buffer.

Following three PBS washes, cells were incubated with species-specific Alexa Fluor-conjugated secondary antibodies (1:500) for 1 h at room temperature protected from light. Cells were counterstained with DAPI (1:2,000) for 5 min, washed twice with PBS, and imaged at 10× magnification using a Molecular Devices ImageXpress high-content imaging system.

Images were post-processed in ImageJ and analyzed using Google Colab and CellProfiler. DAPI-positive nuclei were segmented in Colab to generate a nuclear mask, which was subsequently used in CellProfiler for marker quantification. For HB9-stained cultures, ISL1/HB9 double-positive nuclei were quantified, while ISL1 and CHX10 positivity were assessed individually in CHX10-stained cultures. Neural progenitor cells, which do not express neuronal markers, were used as a biological negative control to establish fluorescence thresholds distinguishing autofluorescence from true-positive staining. Data were plotted in R.

Multielectrode array (MEA) electrophysiology study

Every other day beginning on Day 24 of the overall protocol, or 2 days following cell seeding on MEA plates and the beginning of maturation, recordings were performed. These recordings were performed on alternating days with feedings so as not to interfere with spontaneous neuronal activity. MEA plates were placed in the Axion Biosystems Maestro Edge MEA set to 37ºC and 5% CO_2. Using AxIS Navigator software on the "Spontaneous + Viability"

data acquisition setting, live play was run for 3 minutes such that any non-representative spontaneous activity attributed to moving cell plates from their incubator to the MEA would not appear in the recording data file. Following 3-minute play time, data recording began. MEA software captured average impedance (kΩ) per well as a proxy for average viability. Spontaneous electrophysiological activity was recorded for 10 minutes uninterrupted. Following 10-minute spontaneous recording, recording was paused and data acquisition setting changed to "Electrically evoked." The stimulation paradigm was set to deliver 5 pulses at a 1 Hz frequency, each pulse containing 3 stimuli of 0.6V, 400 μs, and 50 μA. This stimulation was delivered to the bottom right corner large electrode on the MEA plate only to best observe signal propagation. After starting a new evoked recording file, the "Start" button was pushed to deliver this stimulation to each well. This process was repeated 10 times per recording. Following the conclusion of this recording, plates were removed from the MEA interface and returned to incubation.

Results & Discussion

The first aim of this project was to generate hindbrain-region motor neurons from control Kolf2.1J, FUS, and SOD1 iPSC lines. Figure 1A shows a detailed timeline of the protocol used to generate motor neurons from the neuromesodermal progenitor (NMP) stage through neuronal maturation. As the scope of this project focuses solely on the ventral progenitor to motor neuron induction and maturation stages, these steps are highlighted in a purple box in the figure. Figure 1B shows representative brightfield images highlighting cell morphology at various key steps of the differentiation protocol. Day 15 represents the beginning of motor neuron induction, where cells are round and compact, still resembling ventral progenitors, and have not yet extended neurites. By day 21, nearing the end of the motor neuron induction phase, neurites have begun to extend in all directions, indicating immature motor neuron presence. These neurites are relatively short and simple, lacking complex branching indicative of a mature neural network, and soma are small. Day 36 represents two weeks of motor neuron maturation, where soma have grown and begun to aggregate in clumps. Neurites have grown extensively in length and complexity, forming a coordinated neural network. Axons have also begun to fasciculate, or form bundles. This day represents the most mature motor neurons attainable in 2-D culture before cells begin to clump extensively and lift from their adhesive substrate.

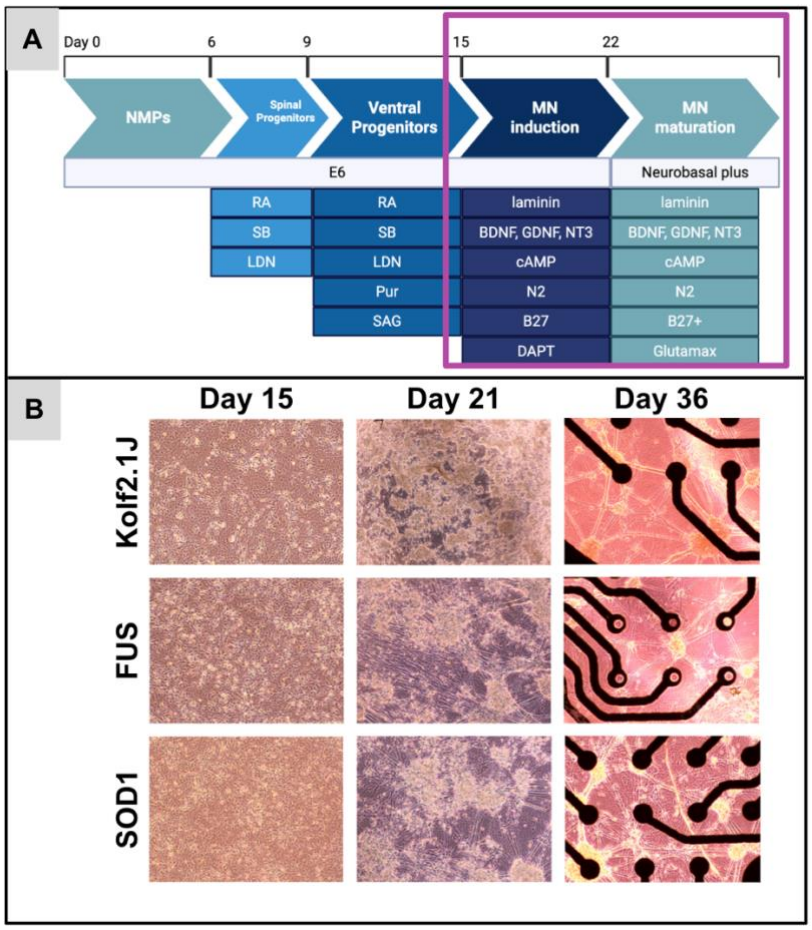

Figure 1. Motor neuron differentiation from ventral progenitors. *(A) Timeline of motor neuron generation with media components. The portion of the differentiation protocol of concern for this project is highlighted in the purple box; (B) Representative brightfield images of cells at various points of protocol including beginning of neuronal induction (Day 15), end of neuronal induction (Day 21), and after two weeks of maturation (Day 36). Days 15 and 21 imaged at 4x magnification; Day 36 imaged at 10x magnification.*

Though morphology as shown in brightfield images suggests the successful production of motor neurons from ventral progenitors, morphological clues alone are not a sure indicator of cell identity. For this reason, we performed ICC staining and imaging, followed by quantification of key markers to verify success and efficiency of differentiation. Before producing neurons, ventral progenitor identity needed to be confirmed, as more dorsal progenitor cells give rise to different subtypes of neurons, while only ventral progenitors may precede motor neurons. Olig2, a transcription factor promoting neurogenesis in the pMN (motor neuron progenitor) domain in the ventral spine, and NKX6.1, a homeobox gene-encoded transcription factor expressed more broadly in the ventral neural tube, were chosen for this purpose[29,30]. All three genotypes showed near-total, 99.9% Olig2 positivity, while NKX6.1 positivity was high in Kolf2.1J and FUS lines (93.4% and 90.6% respectively), but notably lower in SOD1 ventral progenitors at 76.4% (*Fig.*

2B). NKX6.1 expression is contingent on sustained Sonic hedgehog (Shh) and Gli signaling activity, two pathways involved in dorsal-ventral patterning that can be significantly impacted by oxidative stress[30,31]. Pathogenic SOD1 mutations are known to cause oxidative stress early relative to other ALS mutations, as SOD1 protein is an antioxidant enzyme whose functional failure results in rapid accumulation of reactive oxygen species[32]. In contrast, pathogenic FUS mutations affect cells' ability to clear oxidative stress that naturally builds up over time, but do not contribute to its initial buildup[33]. This may mean that the SOD1-mutated cells are experiencing more oxidative stress than FUS at the early progenitor stages, which may impact their Shh/Gli signaling pathways and may present a possible explanation for reduced NKX6.1 expression relative to the other lines. Despite this lowered ventralization efficiency for SOD1 progenitor cells, an overall majority Olig2 and NKX6.1 positivity was sufficient to proceed with further differentiation to motor neurons, with the caveat that the protocol for generating SOD1 mutant ventral progenitors may need to be optimized for future experiments. Additionally, this data represents conditions with single replicates and no statistical comparison; differences in genotypes should be considered preliminary.

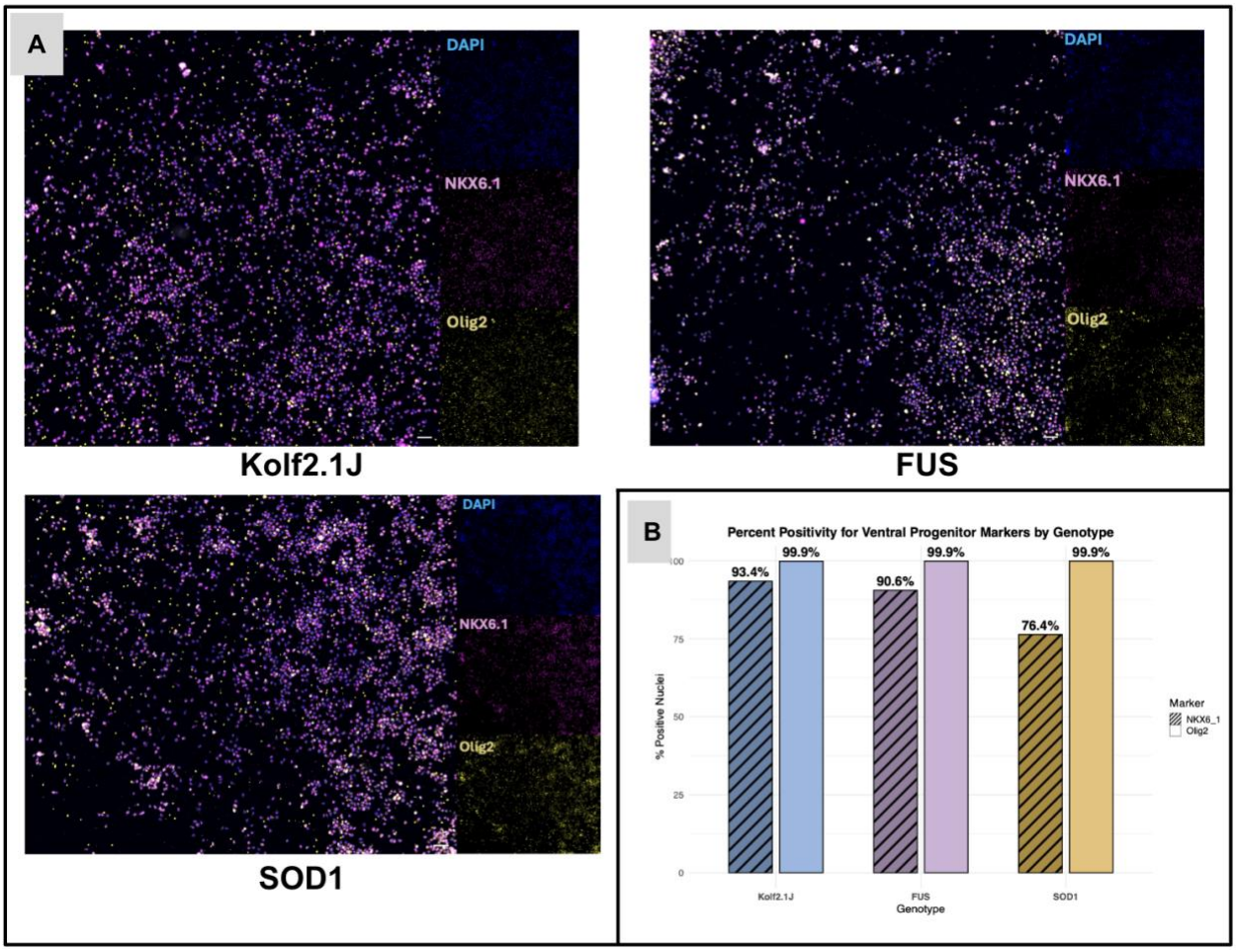

Figure 2. Ventral progenitor marker positivity shows efficient ventralization. *(A) ICC staining (10x magnification) of ventral progenitors for NKX6.1 (magenta), and Olig2 (yellow. Scale bar*

= 50 µm; (B) quantification of NKX6.1 and Olig2 as percent positivity out of DAPI-positive cells. N = 1 replicate per condition; no statistics run. Quantification performed using CellProfiler pipeline (Table 1).

After verifying efficient ventralization and proceeding with neuronal induction and maturation, the subsequent validation step was to use ICC staining to evaluate motor neuron cultures' relative maturity and differentiation efficiency. This was done 13 days following the onset of neural induction, or day 28 of the overall protocol, 6 days into maturation. Markers choline acetyltransferase (ChAT) and class III β-tubulin, also known as Tuj1, are used to visualize neuron processes; ChAT marks the enzyme used to synthesize neurotransmitters in axon fibers of cholinergic neurons, and Tuj1 marks cytoskeletal proteins abundant in neurites in all neuron subtypes[34,35]. These markers are not quantified as they are cytoplasmic and do not allow for accurate cell counting. Islet-1 (ISL1) is a vital transcription factor and nuclear marker essential for progenitors to adopt a motor neuron fate, and it is present beginning at neuron induction, meaning it should mark all motor neurons regardless of maturity[36]. Hb9, or Mnx1, is a nuclear transcription factor specific to post-mitotic motor neurons fully committed to the motor neuron fate, marking only mature motor neurons[37]. Thus, as shown in *Fig. 3A*, ISL1/Hb9 co-positivity quantification is used to estimate, out of all motor neurons or pre-motor neurons present, what proportion is mature. Both Kolf2.1J and FUS lines show high maturity, with 82.2% and 83.9% Hb9/ISl1 co-positivity respectively, but SOD1 drops dramatically to 34.1%. This result, following low NKX6.1 expression in SOD1 seen in *Fig. 2B* potentially suggests that a partially-ventralized progenitor pool produces an even less efficient mature motor neuron pool downstream. Alternatively, the SOD1 mutation could still be delaying development and diluting maturation; either way, the fact that SOD1 motor neurons appear to be maturing differently from the other lines adds an additional layer of consideration to all subsequent MEA data analysis. Chx10, also known as Vsx2, is the primary determinant transcription factor for V2a excitatory interneurons, a supporting neuron type that commonly contaminates motor neuron cultures due to the two progenitor domains being adjacent[27]. As shown in *Fig. 3B*, Chx10 is quantified as an inverse measure of purity; the more Chx10+ interneurons, the less pure the culture. Of all DAPI-positive cells, Kolf2.1J is 98.5% ISL1+ and 0.2% Chx10+; FUS is 92.6% ISL1+ and 7.4% Chx10+; and SOD1 is 88% ISL1+ and 11.2% Chx10+. While this result does show relatively high motor neuron purity in all cultures, Chx10 positivity is elevated in both ALS lines relative to the control, meaning these cultures have more excitatory interneurons promoting firing and network connectivity, which could potentially accentuate the appearance of the hyperactive phenotype; this is discussed further in the conclusion section. As these results represent single biological replicates without statistical comparison, differences between genotypes should be regarded as preliminary.

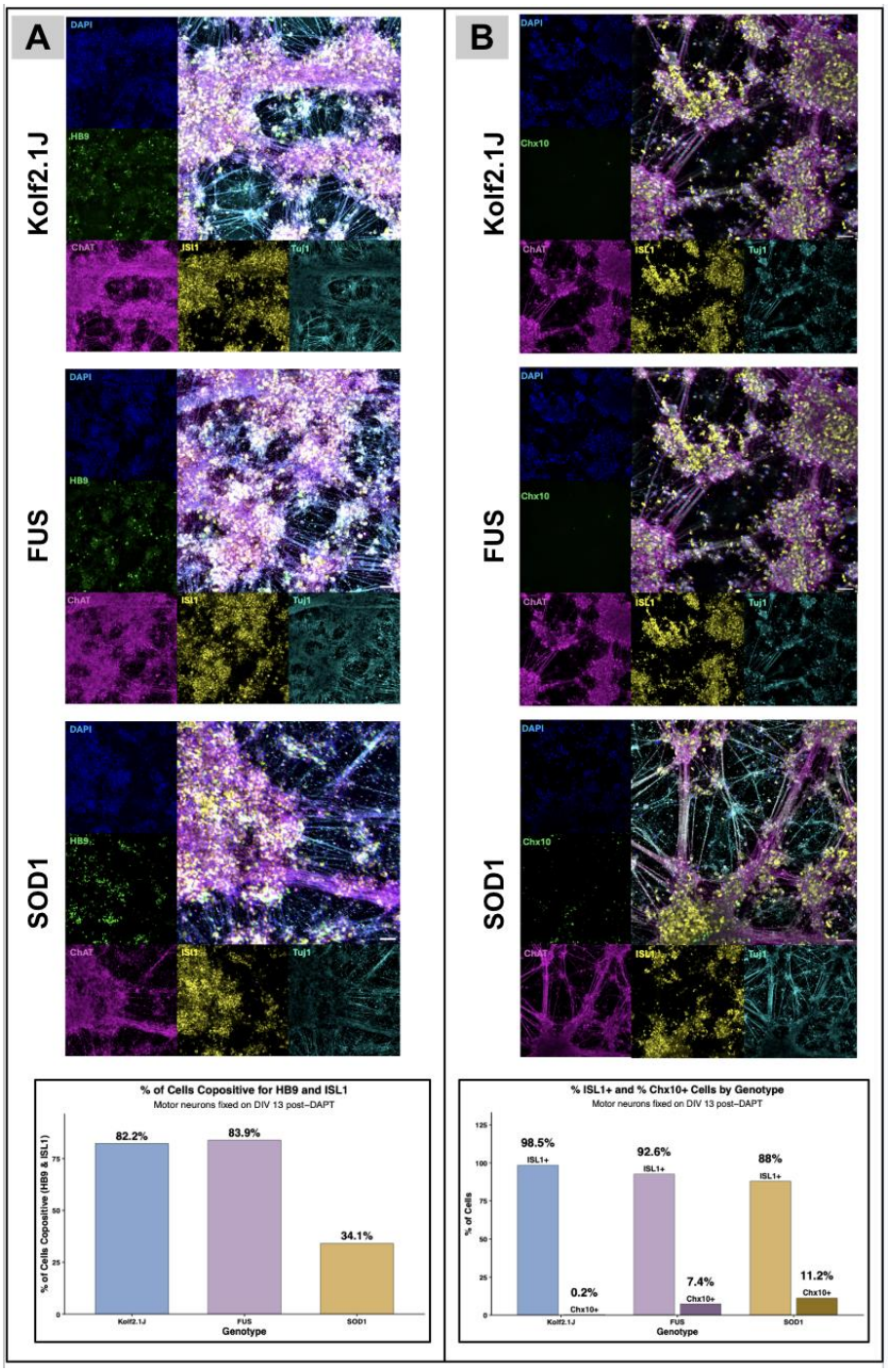

Figure 3. Motor neuron staining suggests culture maturity and purity. *(A) ICC staining (20x magnification, scale bar = 50 µm) of mature motor neurons for Hb9 (green), ChAT (magenta), ISL1 (yellow), and Tuj1(cyan) with corresponding Hb9/ISL1 co-positivity quantification; (B) ICC staining (20x magnification, scale bar = 50 µm) of mature motor neuron cultures for Chx10 (green), ChAT, ISL1, and Tuj1 with corresponding Chx10 positivity quantification. N = 1 replicate per condition; no statistics run. Quantifications performed using CellProfiler pipeline (Table 1).*

Having established mostly mature and pure motor neuron cultures with ICC staining, we then moved to measuring disease-relevant electrophysiology phenotypes with MEA. *Fig. 4 A-F* show various activity metrics from 10-minute spontaneous recordings over the course of 14 days. Mean firing rate (*Fig. 4A*) measures the average number of electrical spikes fired per second across the whole well, weighted according to which electrodes have better cell coverage; this is a blanket measure of electrical activity. No significant effect was observed, though ALS lines trend higher than control. Number of bursts (*Fig. 4B*) quantifies raw number of bursts, or clusters of electrical spikes separated by gaps in activity. No significant effect was observed, though ALS lines again trend higher than control. Burst frequency (*Fig. 4C*) measures bursts per second; examining differences in firing rate and burst frequency together can confer information about the duration of bursts or spike density within bursts, which can imply mechanistic changes in ion dynamics affecting how easily networks initiate and terminate the bursting state. Again, no significant differences observed, though ALS lines trend higher than control. Burst percentage (*Fig. 4D*) measures what proportion of all spikes were part of a burst rather than isolated activity; this gives insight on the relative organization versus randomness of electrical activity. No significant effect was observed. Number of network bursts (*Fig. 4E*) measures network bursts, or bursts where many electrodes across the well fire together as a coordinated group, implying network synchrony. For this metric, trajectories differ significantly (Treatment × DIV $p < 0.05$); control neurons remain relatively unsynchronized throughout the time course, while ALS neurons appear to become hypersynchronous over time, especially SOD1. This implication is fortified with the width at half height of the cross-correlation function, measuring how tightly timed, as opposed to randomly dispersed, synchronous activity is. Lower values indicate synchronous activity takes place in a precise time window, while a higher value indicates a time lag between synchronous action potentials. Trajectories differ significantly here (Treatment × DIV $p < 0.0001$), with both ALS lines losing time precision near DIVs 6-8, then re-gaining it for the remaining data collection time. On the other hand, control neurons continually lose precision over the entire time course. Without other metrics to confirm any mechanistic explanation for this trend, we cannot make a claim as to what causes this difference, but we can say that ALS neurons appear to follow significantly different maturation timelines and patterns of network synchrony development; future experiments to closely probe synchrony are warranted. Weighted mean resistance (*Fig. 4G*) is a proxy for cell viability, normalized to active electrodes; this is considered only to ensure neurons are alive and activity is real; the aim of this project is to quantify disease phenotypes rather than cell death. Notably, the number of technical replicates per condition varies dramatically due to cell death and detachment over the course of data collection (N = 5 Kolf2.1J, 4 FUS, 10 SOD1 wells). This is a real imbalance than impacts our weighting of genotype-specific findings.

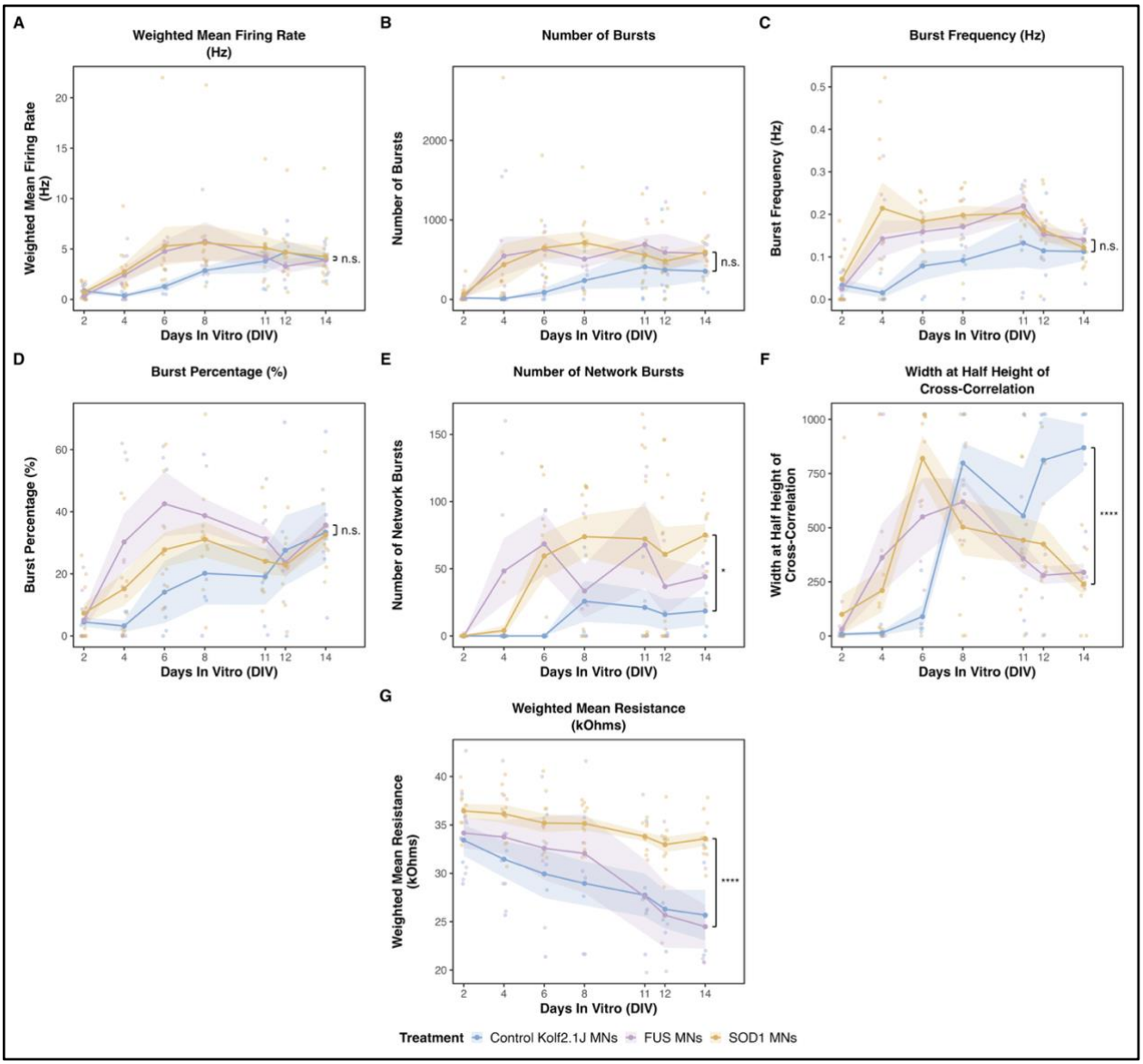

Figure 4. Selected longitudinal MEA spontaneous activity metrics across motor neuron networks (DIV 2-14). *Panels show (A) Weighted mean firing rate; (B) number of bursts, (C) burst frequency, (D) burst percentage, (E) number of bursts, (F) width at half height of the cross-correlation function (a measure of temporal precision of coordinated network activity), and (G) weighted mean resistance, a proxy for viability. Lines represent group mean at each timepoint; shaded bands represent ± SEM; individual points represent values from single wells. Linear mixed-effects model (Value ~ Treatment × DIV + (1 | Well)) fit to test significant trajectory divergence over data collection period. Bracket and asterisks denote significance of the Treatment × DIV interaction term (omnibus test across all three genotypes; n.s. = not significant, *p<0.05, ****p<0.0001). N = 5 Kolf2.1J; 4 FUS; 10 SOD1.*

Spontaneous MEA data is useful for tracking intrinsic network activity and baseline health, but it cannot control for differences across wells in baseline excitability or other factors.

Electrically evoking neuron networks with a uniform stimulus and observing the aftereffects can be a valuable complement. This allows for inter-well comparisons for how strongly and precisely networks respond to the same external input, independent of intrinsic activity, which can elucidate differences in networks' ability to initiate, terminate, or recover following stimulus. The significant result distinguishes SOD1 from control neurons, but not from FUS, meaning that although it can elucidate SOD1-ALS-specific mechanisms, it cannot contribute to the initial question of genotype-region matching. This may also be a statistical artifact of SOD1 having twice as many replicates as other genotypes. Peri-stimulus time histograms (PSTHs) (*Fig. 5A,B)* show the average spiking response per 1 ms for the 15 ms immediately following the onset of stimulation with a set paradigm (5 pulses at a 1 Hz frequency, each pulse containing 3 stimuli of 0.6V, 400 μs, and 50 μA; delivered 10 times per recording) at DIV 6 and DIV 14, respectively. At both timepoints, all three genotypes follow a standard shape: a small peak shortly following stimulation onset, followed by a larger peak around 5 ms post-onset. Divergence between genotypes occurs after this large peak: control (Kolf2.1J) and FUS networks rapidly decayed to their baseline after the second peak at both timepoints. SOD1 networks, on the other hand, show a slower decay and persistent spike elevation for several ms after the large spike. This pattern was more pronounced on DIV 14. This qualitative difference in shape was reflected in the area under the curve (AUC) comparisons (*Fig. 5C,D*), quantifying total spiking in that post-stimulus time frame. At DIV 6, a one-way ANOVA revealed a significant effect of genotype on AUC ($F(2,16) = 4.86$, $p = 0.022$), with the post-hoc comparisons revealing that SOD1 networks showed greater evoked response than control ($p < 0.05$). FUS did not differ from either other genotype at this point. At DIV 14, the same overall pattern was apparent, but the omnibus ANOVA did not reach significance ($F(2,16) = 3.17$, $p = 0.069$), and no pairwise comparisons were significant. Taken together, slower decay and elevated AUC in SOD1 networks suggests that these fail to terminate their response to external stimulation as efficiently as control or FUS networks, particularly at DIV 6. This is consistent with the documented hyperexcitability phenotype, in which impaired repolarization or dysregulation in inhibitory activity leaves the network unable to properly return to baseline polarity following stimulus. In our data, this phenotype was specific to SOD1 relative to control, and FUS did not show the same pattern.

Considered alongside spontaneous activity data, this evoked-response data reinforces a pattern emerging across both MEA assays: ALS genotypes, especially SOD1, show clear evidence of network electrophysiological dysfunction relative to healthy neurons, supporting the validity of our model for detecting disease-relevant phenotypes generally. However, neither spontaneous nor evoked data could distinguish FUS and SOD1 on any metric tested, leaving our initial hypothesis neither confirmed nor rejected. Repetition of this MEA experiment with more statistical power, as well as other functional assays to examine other mechanistically implicated properties of neuron health, such as metabolism, could illuminate more differences yet uncovered. Further, because differentiation purity varied across genotypes, particularly for SOD1, we cannot fully exclude the possibility that these differences are attributed to culture composition rather than intrinsic pathology; repetition with a purer culture would be beneficial.

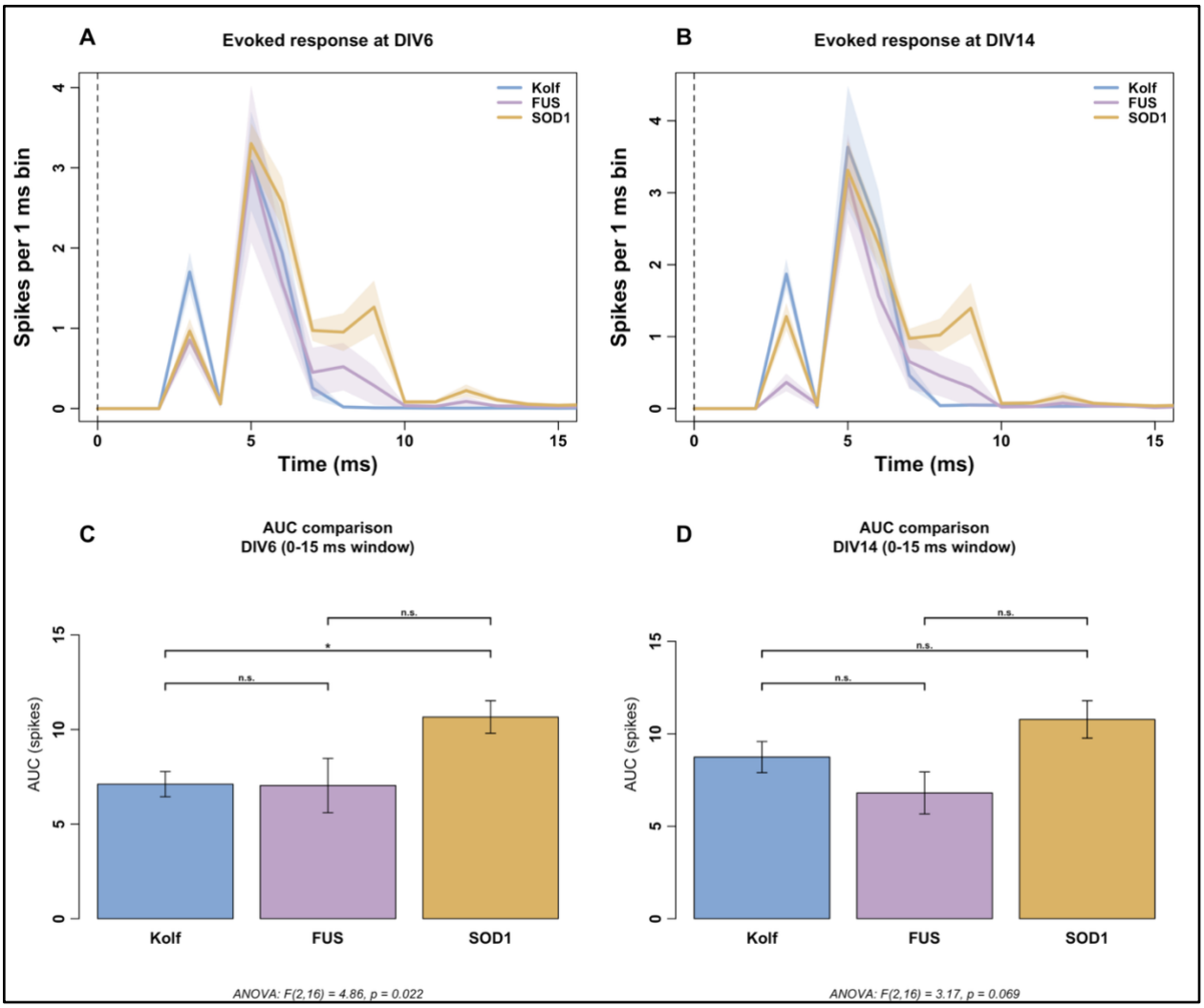

Figure 5. Evoked network responses of motor neuron networks at DIV 6 and DIV 14. *Panels show (A) peri-stimulus time histogram (PSTH) of evoked response at DIV 6; (B) PSTH of the evoked response at DIV 14; (C) area under the curve (AUC) of evoked response at DIV 6 as plotted in (A); (D) AUC of evoked response at DIV 14 as plotted in (B). Lines in (A,B) represent group mean per 1 ms; shaded bands represent ± SEM. Bars in (C,D) represent group mean AUC; error bars represent ± SEM across wells. One-way ANOVA with Tukey's post-hoc test was performed at each DIV to test for significant differences in AUC by genotype. Brackets and asterisks denote significance of pairwise Tukey comparisons (n.s. = not significant, * = p < 0.5). N = 5 Kolf2.1J; 4 FUS; 10 SOD1.*

Conclusion

This project aimed to generate hindbrain-patterned motor neurons from a parent line and two ALS-associated mutant lines in order to more accurately model bulbar-onset ALS and investigate the effects of genotype on disease-relevant electrophysiological phenotypes as measured with MEA assays. We achieved successful generation and validation of hindbrain-

patterned motor neurons with minimal supporting cells across all three genotypes, though there remains room for optimization, especially in the SOD1 mutant line. We successfully collected MEA data across 14 days for both spontaneous network activity and network activity when electrically evoked. Though minimal significant differences were observed between ALS genotypes in spontaneous MEA data, early hyperactive phenotypes are observed in both ALS genotypes relative to control motor neurons, as seen through number of network bursts (*Fig. 4E*). Data also suggests that ALS-afflicted motor neurons follow a different maturation trajectory compared to controls, with the temporal dynamics of coordinated network activity differing significantly, as shown through width at half height of cross-correlation data. Finally, SOD1 motor neurons appear visually to have a prolonged response to electrical stimulation compared to other lines, suggesting that these neurons fail to cleanly terminate network responses, though the mechanism behind this is unclear.

We hypothesized that bulbar ALS-associated FUS mutation would cause more severe disease phenotypes when paired with bulbar-region motor neurons compared to the mismatched spinal-associated SOD1 mutation. Currently, the data collected does not support this claim; no meaningful differences between FUS and SOD1 mutant lines were uncovered in any of the MEA metrics. This could be explained by many factors. Most notably, neurons lifted off of MEA electrodes following 14 days of data collection, confounding any future findings and forcing the end of data collection. This is a relatively short timescale for neuronal network maturation, and it could be that the neurons simply were not mature enough for differences in disease-relevant phenotypes to be observable, especially since the effects of FUS mutations are expected to arise later in maturation than SOD1. We did, however, observe differences in activity for the two ALS genotypes compared to the control model, showing early signs of the hyperactivity phenotype well-documented in literature for both FUS and SOD1-ALS. This finding supports the validity of our bulbar-region motor neuron model for capturing network-level, disease-relevant electrophysiology signatures in a general sense, conferring confidence in the model for future experiments. Due to our limited sample size, a lack of measurable distinction between FUS and SOD1 phenotypes should be considered inconclusive rather than an absence of genotype effect. This question should be studied further with larger sample sizes and more experiments.

In addition to the limitations already noted (electrode detachment limiting data collection; small MEA sample size), several other limitations limit our interpretation of the model and warrant further investigation. First, as mentioned, differentiation of SOD1 cells into motor neurons was considerably less efficient than other lines beginning in the ventral progenitor stage, leading to lowered NKX6.1 expression and later, lower HB9/ISL1 co-positivity for these cells. This could potentially be attributed to the SOD1 mutation effects blocking the Shh signaling molecules used to support ventral patterning in the progenitor stages, implying that protocol optimization is necessary to achieve total ventralization and a pure motor neuron culture for this line, perhaps with an altered Shh dosing timeline; simply raising the dose of morphogen treatment could become cytotoxic or could push ventral progenitors towards an oligodendroglial fate rather than neuronal[38]. Additionally, both ALS neuron cultures had more Chx10+ excitatory

interneurons compared to controls, which may exacerbate evidence of the ALS-associated hyperactivity phenotype, as excitatory interneurons would accentuate network activity. This could relate, again, to the need to optimize ventralization and neuron induction protocols; cells that do not effectively commit to the ventral domain, or later to the neuronal fate, may instead become excitatory interneurons, as the p2 (excitatory interneuron) domain falls just dorsal to the pMN (motor neuron) domain in the Shh signaling gradient[25].

In order to build on this work, we have identified several key next steps for improving upon our model and further testing genotype-region interactions in ALS. First and foremost, we aim to develop a parallel model for spinal-onset ALS using more caudal, spinal cord-patterned motor neurons. By deriving motor neurons from the same three cell lines (Kolf2.1J, FUS, and SOD1) with a lower spinal identity, we hope to test the other side of our hypothesis: will SOD1, the spinal-associated mutation, cause more severe disease phenotypes in spinal neurons compared to FUS, the bulbar-associated mutation? Additionally, to improve upon our model and extend the period of data collection past 14 days, we hope to incorporate 3-dimensional spheroid culture models for our motor neurons; as motor neuron processes tend to naturally extend in 3D as they mature, we believe that creating a system to support them in growing naturally will alleviate the plate detachment issues observed in 2D[39]. Lastly, we hope to incorporate additional ALS-associated genotypes such as TDP-43 or C9orf72 in order to improve documentation of *in-vitro* phenotypes and contribute to an overall goal of characterizing ALS subtypes. Ultimately, as region-specific iPSC models remain rare in the ALS field, this work represents an early but meaningful step towards closing that gap, laying foundations for future work and eventually drug screening strategies capable of addressing bulbar-onset ALS and answering the greater question: why is bulbar-onset ALS so much more aggressive than other types?

Table 1. Key Resources.

REAGENT or RESOURCE	SOURCE	IDENTIFIER
Antibodies		
Anti-Olig2 (rabbit)	Millipore	Cat#AB9610
Anti-NKX6.1 (goat)	R&D Systems	Cat#AF5857
Anti-Hb9 (mouse)	DSHB	Cat#81.5C10-c
Anti-Isl1 (goat polyclonal)	R&D Systems	Cat#AF1837
Anti-Tuj1 (chicken polyclonal)	Novus Biologicals	Cat#NB100-1612

REAGENT or RESOURCE	SOURCE	IDENTIFIER
Anti-ChAT (rabbit)	Abcam	Cat#ab181023
Anti-Chx10 (mouse)	SCBT	Cat#sc-365519
Donkey anti-mouse IgG Alexa Fluor 488	Thermo Fisher Scientific	Cat#A-21202
Donkey anti-rabbit IgG Alexa Fluor 555	Thermo Fisher Scientific	Cat#A-31572
Donkey anti-goat IgG Alexa Fluor 647	Thermo Fisher Scientific	Cat#A-21447
Donkey anti-chicken IgG Alexa Fluor Plus 594	Thermo Fisher Scientific	Cat#A78951
Chemicals, peptides, and recombinant proteins		
Chroman 1 (CEPT cocktail component, 50 nM)	Tocris	Cat#7163
Emricasan (CEPT cocktail component, 5 μM)	Selleck Chemical	Cat#50-136-5235
Polyamine supplement (CEPT cocktail component, 1:1,000)	Tocris	Cat#77391PACK
trans-ISRIB (CEPT cocktail component, 0.7 μM)	Tocris	Cat#5284
Recombinant human GDNF (10 ng/mL)	The Well Bioscience	Cat#CG092-B
Recombinant human BDNF (10 ng/mL)	The Well Bioscience	Cat#CG002-B

REAGENT or RESOURCE	SOURCE	IDENTIFIER
Recombinant human NT-3 (10 ng/mL)	The Well Bioscience	Cat#11563-N3
Cyclic AMP (cAMP, 10 μM)	Sigma-Aldrich	Cat#D0260-5MG
DAPT (γ-secretase inhibitor, 10 μM)	Sigma-Aldrich	Cat#26-341-0
AraC (cytosine arabinoside, 10 μM)	Sigma-Aldrich	Cat#C6645-25MG
Insulin solution, human (100 μL per 500 mL E6; 2 μg/mL final)	Sigma-Aldrich	Cat#I9278
Transferrin, human (500 μL of 10 mg/mL per 500 mL E6; 1 μg/mL final)	Sigma-Aldrich	
Laminin (1 μg/mL for neural induction media; 2 μg/mL for plate coating)		
Glutamax		
Matrigel (plate coating)		
Poly-D-Lysine (PDL, 100 μg/mL) (plate coating)		
Accutase	Thermo Fisher Scientific	Cat#A6964-500ML
Papain (for MN dissociation)	Worthington	Cat#LK003178
DNase I (for MN dissociation)	Worthington	Cat#LK003172

REAGENT or RESOURCE	SOURCE	IDENTIFIER
Fetal bovine serum		
DAPI	Invitrogen	Cat#D1306
Paraformaldehyde, 16% stock (diluted to 4% working solution)	Electron Microscopy Sciences / Thermo Fisher Scientific	
Normal donkey serum	Sigma-Aldrich	Cat#S30-100ML
Triton X-100	Sigma-Aldrich	
DMEM/F12, HEPES (E4/E6/E8 base; also MN induction media)	Thermo Fisher Scientific	Cat#11330057
L-Ascorbic acid 2-phosphate sesquimagnesium salt hydrate (E4/E6/E8 component, 0.2 mg/mL)	Sigma-Aldrich	Cat#A8960-5G
Sodium selenite (E4/E6/E8 component)	Sigma-Aldrich	Cat#214485-100G
Sodium bicarbonate (E4/E6/E8 component)	Sigma-Aldrich	Cat#S3817-500G
Neurobasal-A medium (MN maturation media base)	Thermo Fisher Scientific	Cat#10888022
B27 supplement (2%; MN induction media)	Thermo Fisher Scientific	Cat#A3582801
B27 Plus Supplement (2%; MN maturation media)	Thermo Fisher Scientific	Cat#A3582801

REAGENT or RESOURCE	SOURCE	IDENTIFIER
N2 supplement (1%; OPC and MN induction media)	Thermo Fisher Scientific	Cat#17502001
Deposited data		
Custom Python image analysis pipeline (MN quantification, Google Colab then CellProfiler)	Nicole Teaney	Google Colab CellProfiler Pipeline
Custom CellProfiler image analysis pipeline (VP quantification, CellProfiler)	Patrick J. Flynn	CellProfiler Pipeline
Experimental models: Cell lines		
Kolf2.1J human induced pluripotent stem cells (WT)	The Jackson Laboratory	JIPSC001000
Kolf2.1J human induced pluripotent stem cells; FUS R495X CRISPR-edited (SNV/WT)	The Jackson Laboratory	JIPSC001004
Kolf2.1J human induced pluripotent stem cells; SOD1 A5V CRISPR-edited (REV/WT)	The Jackson Laboratory	JIPSC001572
Software and algorithms		
R (v4.4.2)	R Core Team	https://www.r-project.org/; RRID:SCR_001905
CellProfiler (v4)	Carpenter et al.	https://cellprofiler.org/; RRID:SCR_007358

REAGENT or RESOURCE	SOURCE	IDENTIFIER
Google Colab (GPU-accelerated pipeline execution)	Google	https://colab.research.google.com/
Other		
Molecular Devices ImageXpress Micro Confocal (high-content imaging)	Molecular Devices	
Axion Biosystems Maestro Edge Multielectrode Array	Axion Biosystems	
Lumos MEA 24-well plate	Axion Biosystems	
Ultra-low attachment 6-well plates	Corning	
Ultra-low attachment 12-well plates	Corning	

References

1. Hu, Y. *et al.* Pathological mechanisms of amyotrophic lateral sclerosis. *Neural Regen. Res.* **19**, 1036–1044 (2023).
2. Masrori, P. & Van Damme, P. Amyotrophic lateral sclerosis: a clinical review. *Eur. J. Neurol.* **27**, 1918–1929 (2020).
3. Traxinger, K., Kelly, C., Johnson, B. A., Lyles, R. H. & Glass, J. D. Prognosis and epidemiology of amyotrophic lateral sclerosis. *Neurol. Clin. Pract.* **3**, 313–320 (2013).
4. Larson, T. C. *et al.* Causes of death among United States decedents with ALS: An eye toward delaying mortality. *Ann. Clin. Transl. Neurol.* **10**, 757–764 (2023).

5. Requardt, M. V., Görlich, D., Grehl, T. & Boentert, M. Clinical Determinants of Disease Progression in Amyotrophic Lateral Sclerosis—A Retrospective Cohort Study. *J. Clin. Med.* **10**, 1623 (2021).
6. Kim, S., Kim, D. K., Jeong, S. & Lee, J. The Common Cellular Events in the Neurodegenerative Diseases and the Associated Role of Endoplasmic Reticulum Stress. *Int. J. Mol. Sci.* **23**, 5894 (2022).
7. Stegmann, G. M. *et al.* Early detection and tracking of bulbar changes in ALS via frequent and remote speech analysis. *Npj Digit. Med.* **3**, 132 (2020).
8. Zoccolella, S. *et al.* Analysis of survival and prognostic factors in amyotrophic lateral sclerosis: a population based study. *J. Neurol. Neurosurg. Psychiatry* **79**, 33–37 (2008).
9. Shellikeri, S. *et al.* The Neuropathological Signature of Bulbar-onset ALS: A Systematic Review. *Neurosci. Biobehav. Rev.* **75**, 378–392 (2017).
10. Wang, H., Guan, L. & Deng, M. Recent progress of the genetics of amyotrophic lateral sclerosis and challenges of gene therapy. *Front. Neurosci.* **17**, (2023).
11. Nijs, M. & Van Damme, P. The genetics of amyotrophic lateral sclerosis. *Curr. Opin. Neurol.* **37**, 560–569 (2024).
12. Miller, T. M. *et al.* Trial of Antisense Oligonucleotide Tofersen for SOD1 ALS. *N. Engl. J. Med.* **387**, 1099–1110 (2022).
13. Blair, H. A. Tofersen: First Approval. *Drugs* **83**, 1039–1043 (2023).
14. Kelly, T. K., Karsten, S. L., Geschwind, D. H. & Kornblum, H. I. Cell Lineage and Regional Identity of Cultured Spinal Cord Neural Stem Cells and Comparison to Brain-Derived Neural Stem Cells. *PLoS ONE* **4**, e4213 (2009).

15. Sagner, A. & Briscoe, J. Establishing neuronal diversity in the spinal cord: a time and a place. *Development* **146**, dev182154 (2019).

16. Siebert, J. R., Kennedy, K. & Osterhout, D. J. Neurons Are Not All the Same: Diversity in Neuronal Populations and Their Intrinsic Responses to Spinal Cord Injury. *ASN NEURO* **17**, 2440299.

17. Gao, Y. *et al.* Altered Inflammatory Signature in a C9ORF72 -ALS iPSC-Derived Motor Neuron and Microglia Coculture Model. *Glia* **74**, e70084 (2026).

18. Ferraiuolo, L. *et al.* Oligodendrocytes contribute to motor neuron death in ALS via SOD1-dependent mechanism. *Proc. Natl. Acad. Sci. U. S. A.* **113**, E6496–E6505 (2016).

19. Gagliardi, D. *et al.* Clinical and molecular features of patients with amyotrophic lateral sclerosis and SOD1 mutations: a monocentric study. *Front. Neurol.* **14**, 1169689 (2023).

20. Moens, T. G. *et al.* Amyotrophic lateral sclerosis caused by *FUS* mutations: advances with broad implications. *Lancet Neurol.* **24**, 166–178 (2025).

21. Shaker, M. R. *et al.* Anteroposterior Wnt-RA Gradient Defines Adhesion and Migration Properties of Neural Progenitors in Developing Spinal Cord. *Stem Cell Rep.* **15**, 898–911 (2020).

22. Rifes, P. *et al.* Modeling neural tube development by differentiation of human embryonic stem cells in a microfluidic WNT gradient. *Nat. Biotechnol.* **38**, 1265–1273 (2020).

23. Andrews, M. G., Kong, J., Novitch, B. G. & Butler, S. J. New perspectives on the mechanisms establishing the dorsal-ventral axis of the spinal cord. *Curr. Top. Dev. Biol.* **132**, 417–450 (2019).

24. Crawford, T. Q. & Roelink, H. The notch response inhibitor DAPT enhances neuronal differentiation in embryonic stem cell-derived embryoid bodies independently of sonic hedgehog signaling. *Dev. Dyn. Off. Publ. Am. Assoc. Anat.* **236**, 886–892 (2007).

25. Novitch, B. G., Chen, A. I. & Jessell, T. M. Coordinate Regulation of Motor Neuron Subtype Identity and Pan-Neuronal Properties by the bHLH Repressor Olig2. *Neuron* **31**, 773–789 (2001).

26. Amoroso, M. W. *et al.* Accelerated High-Yield Generation of Limb-Innervating Motor Neurons from Human Stem Cells. *J. Neurosci.* **33**, 574–586 (2013).

27. Clovis, Y. *et al.* Chx10 consolidates V2a interneuron identity through two distinct gene repression modes. *Cell Rep.* **16**, 1642–1652 (2016).

28. Burley, R. & Harvey, J. R. M. Multielectrode Arrays. *Methods Mol. Biol.* **2188**, 109–132 (2021).

29. Sagner, A. *et al.* Olig2 and Hes regulatory dynamics during motor neuron differentiation revealed by single cell transcriptomics. *PLoS Biol.* **16**, e2003127 (2018).

30. Sander, M. *et al.* Ventral neural patterning by Nkx homeobox genes: Nkx6.1 controls somatic motor neuron and ventral interneuron fates. *Genes Dev.* **14**, 2134–2139 (2000).

31. Jing, J. *et al.* Hedgehog signaling in tissue homeostasis, cancers and targeted therapies. *Signal Transduct. Target. Ther.* **8**, 315 (2023).

32. Motataianu, A., Serban, G., Barcutean, L. & Balasa, R. Oxidative Stress in Amyotrophic Lateral Sclerosis: Synergy of Genetic and Environmental Factors. *Int. J. Mol. Sci.* **23**, 9339 (2022).

33. Wang, H. *et al.* Mutant FUS causes DNA ligation defects to inhibit oxidative damage repair in Amyotrophic Lateral Sclerosis. *Nat. Commun.* **9**, 3683 (2018).

34. Lee, S. *et al.* TuJ1 (class III beta-tubulin) expression suggests dynamic redistribution of follicular dendritic cells in lymphoid tissue. *Eur. J. Cell Biol.* **84**, 453–459 (2005).

35. Barber, R. P. *et al.* The morphology and distribution of neurons containing choline acetyltransferase in the adult rat spinal cord: An immunocytochemical study. *J. Comp. Neurol.* **229**, 329–346 (1984).

36. Liang, X. *et al.* Isl1 Is required for multiple aspects of motor neuron development. *Mol. Cell. Neurosci.* **47**, 215–222 (2011).

37. Letchuman, S. *et al.* Transcription Factor Hb9 Is Expressed in Glial Cell Lineages in the Developing Mouse Spinal Cord. *eNeuro* **9**, ENEURO.0214-22.2022 (2022).

38. Danesin, C. *et al.* Ventral Neural Progenitors Switch toward an Oligodendroglial Fate in Response to Increased Sonic Hedgehog (Shh) Activity: Involvement of Sulfatase 1 in Modulating Shh Signaling in the Ventral Spinal Cord. *J. Neurosci.* **26**, 5037–5048 (2006).

39. Spijkers, X. M. *et al.* A directional 3D neurite outgrowth model for studying motor axon biology and disease. *Sci. Rep.* **11**, 2080 (2021).